Materials Today Bio 16 (2022) 100401

Contents lists available at ScienceDirect

Materials Today Bio

journal homepage: www.journals.elsevier.com/materials-today-bio

Light-activated gold nanorods for effective therapy of venous malformation

Yihong Jiang [a], Junchao Liu [a], Jinbao Qin [a], Jiahao Lei [a], Xing Zhang [a,****], Zhijue Xu [a], Weimin Li [a], Xiaobing Liu [a], Ruihua Wang [a,***], Bo Li [a,b,**], Xinwu Lu [a,b,*]

[a] Department of Vascular Surgery, Shanghai Ninth People's Hospital, Shanghai Jiao Tong University School of Medicine, Shanghai, 200011, China
[b] Department of Vascular Surgery, Fengcheng Branch, Shanghai Ninth People's Hospital Affiliated to Shanghai Jiao Tong University School of Medicine, Shanghai, 201411, China

ARTICLE INFO

Keywords:
Venous malformation
Endothelial cell
Gold nanorods

ABSTRACT

Gold nanorods have been studied extensively in the field of tumor therapy but have not been explored in the treatment of venous malformation (VM), which is a common vascular disease in clinic practice lacking an effective therapeutic approach. Herein we reported a nanoplatform of CD31 antibody-conjugated gold nanorods for the photothermal therapy of venous malformation. We immobilized CD31 antibodies on gold nanorods using standard 1-ethyl-3-(3-dimethylaminopropyl) carbodiimide (EDC)/N-hydroxysulfosuccinimide sodium (NHS) amine coupling strategies. Besides, a VM xenograft model suitable for testing therapeutic efficacy was established by isolating and culturing VM patient endothelial cells. In vitro experiments indicated that anti-CD31 gold nanorods (GNRs) combined with photothermal therapy (PTT) contributed to the suppression of proliferation and activation of the apoptosis pathway. For in vivo experiments, anti-CD31 GNRs were locally injected into VM xenograft models followed by near infrared (NIR) 808 nm laser irradiation. Notably, VM on the mice was destroyed and absorbed. The anti-CD31 GNRs nanoplatform may serve as a new strategy for the treatment of VM which is of good biosafety and high value of applications.

1. Introduction

Venous malformation (VM) is the most common type of vascular malformation, with an estimated prevalence of 1% [1,2]. VM consists of dysplastic venous channels, which are usually found in the head, neck, limbs, and trunk [3]. VM patients have extremely different symptoms such as severe pain, impaired joint function, craniofacial implications, episodic bleeding, and cardiac defects, which eventually result in critical conditions [3]. Conventional treatments include medication, interventional management, surgical excision, and laser ablation. Despite personalized multiple strategies being used, micro-venous channels infiltrating into soft tissue cannot be completely excised or cured. Recent studies have shown that pharmacological blockade of signaling pathways may be a feasible strategy. Sirolimus and rapamycin have been tested in patients with slow-flow VM lesions and have achieved some progress [4–6]. However, these medications lack tissue selectivity and generally correlate with serious side reactions, including bone marrow suppression, mouth sores, and metabolic disturbances [7]. The recurrence of VM and multiple complications remain challenges for many patients, and an effective minimally invasive approach is lacking.

Photothermal therapy (PTT) exhibits attractive technological prospects and clinical potentials [8,9]. PTT is an effective, minimally invasive, and high biocompatibility method. Near infrared (NIR) light can be converted into heat energy by photothermal conversion agents, causing multiple cell physiological processes, such as membrane damage, protein degeneration, and cell death [10,11]. Most researches focused on the diagnosis and treatment of tumors using PTT rather than vascular diseases [12–14]. Some works have explored the therapeutic effect of PTT on atherosclerotic diseases by eliminating inflammation and intimal hyperplasia of the vascular system [15,16], while studies that

* Corresponding authors. Department of Vascular Surgery, Shanghai Ninth People's Hospital, Shanghai Jiao Tong University School of Medicine, Shanghai, 200011, China.
** Corresponding author. Department of Vascular Surgery, Shanghai Ninth People's Hospital, Shanghai Jiao Tong University School of Medicine, Shanghai, 200011, China.
*** Corresponding authors.
**** Corresponding author.
E-mail addresses: zhangxing@shsmu.edu.cn (X. Zhang), wangruihua0330@sina.com (R. Wang), boli@shsmu.edu.cn (B. Li), luxinwu@shsmu.edu.cn (X. Lu).

https://doi.org/10.1016/j.mtbio.2022.100401
Received 3 March 2022; Received in revised form 10 August 2022; Accepted 11 August 2022
Available online 18 August 2022

investigated PTT on VM are still missing.

Among photothermal conversion agents, gold nanorods (GNRs) have broad application prospects in nanobiology and biomedicine because of their unique optical activity, simple synthesis method, stable chemical properties, good biocompatibility, and easy surface modification [17–19]. Different organic ligands such as peptides, antibodies, and oligonucleotides can be anchored to the surface of GNRs to achieve various bio-functions [20]. The IgG antibody has been proved to be an eligible agent to promote selective interactions with the targeted cells and cellular uptake. Despite substantial efforts, there is no specific biomarker has been found between venous malformation endothelial cell (VM-EC) and normal endothelial cell (EC) [21,22]. Fortunately, platelet endothelial cell adhesion molecule-1 (CD31) is a marker for EC which is highly expressed in the membrane of VM-ECs, and the CD31 antibody conjugated GNRs may achieve efficient localization in the target tissues [23,24].

To be in accordance with different research purposes, diverse VM models have been established, ranging from those based on venous structures to those based on gene manipulation techniques. However, to our knowledge, no VM model was specifically designed or tested for photothermal therapy research. A VM xenograft model suitable for photothermal therapy research has some requirements, including a stable modeling procedure, suitable size of VM lesions to match laser instruments, and high growth velocity to improve research efficiency. In this work, we isolated and characterized VM-ECs from patient tissues and established a xenograft model of VM which remains the integrity of genetic materials and may be appropriate for PTT research. Besides, we synthesized and characterized the antibody-conjugated GNRs and explored the effectiveness and underlying mechanisms. The synthesized GNRs were first modified with polyethylene glycol (PEG) to avoid nanoparticle agglomeration, and then the CD31 antibodies were conjugated to the surface of the GNRs. Irradiation of 808 nm NIR laser exhibited a synergistic biological effect by promoting apoptosis and inhibiting proliferation on VM-ECs engulfing anti-CD31 GNRs. As far as we know, this research is the first to focus on the PTT of VMs by nanomaterials, which may inspire further research in the photothermal therapy of vascular malformation diseases.

2. Materials and methods

2.1. Synthesis of GNRs

According to the previous protocols, the GNRs were prepared by the seed-mediated method [25,26]. Briefly, cetyltrimethylammonium bromide (CTAB) (5 mL, 0.2 mol L^{-1}) in an aqueous solution and a solution of $HAuCl_4{\cdot}3H_2O$ (10.0 mL, 0.5 mmol L^{-1}) were mixed to prepare the seed solution. Then, a mixture of $NaBH_4$ (1.2 mL, 0.01 mol L^{-1}) and the seed solution was made under stirring and the solution mixture was kept at 27 °C for 2 h without agitating. To prepare the growth solution, following aqueous solutions including $AgNO_3$ (3.0 mL, 4.0 mmol L^{-1}), CTAB (50 mL, 0.2 mol L^{-1}), $HAuCl_{4.3}H_2O$ (100 mL, 1.0 mmol L^{-1}), and ascorbic acid (1.4 mL, 80 mmol L^{-1}) were mixed. To initiate the growth procedure of nanorods, an aliquot (0.12 mL) of the seed solution was added to the growth solution. Afterward, the mixture was stirred for 10 s and was then allowed to stand for 4 h. Finally, the GNRs were collected by centrifugation.

2.2. Synthesis of GNRs-PEG conjugated to CD31 antibody

To prepare gold nanorods attached with PEG, GNRs were transferred into acetate buffer at a pH of 5 containing cetrimonium bromide. After a reaction of 30 min, COOH-PEG-SH was added and the mixture was kept reacting for 90 min. Then, the mixture was transferred into a MES buffer containing NaCl and polysorbate 20 [27]. EDC/NHS linking chemistry was applied for the attachment of GNRs-PEG and CD31 antibodies [27,28]. GNRs-PEG were mixed with an equal volume of 48 mM EDC and 12 mM NHS. After reacting for 15 min, 20 ppm CD31 antibody in MES buffer which contains 120 mM NaCl and 0.005% (v/v) polysorbate 20 were added into the suspension. After 1 h, 10 mM 2-methoxyethylamine was added into the mixture to block unreacted succinimide ester. Finally, the anti-CD31 GNRs were collected into sterile PBS after three cycles of centrifugation. In addition, part of the product was mixed with 5-Carboxyfluorescein (5-FAM) in MES and vortexed overnight under dark conditions. 5-FAM labeled nanorods were harvested by centrifugation for three cycles.

2.3. Materials characterization

Ultraviolet–visible (UV–vis) spectrum and TEM were used to validate that GNRs were synthesized correctly. Ultraviolet–visible absorption spectra were detected on Cary 50 UV–vis spectrometer and TEM (CM12, Philips, the Netherlands) was performed to characterize the size, shape, and morphology of the GNRs. Fourier transform infrared spectroscopy (FTIR) spectra were collected using a Nicolet 6700 FTIR spectrometer (Thermo Scientific, USA). Coomassie staining was performed by the Bio-Safe™ Coomassie stain (BIORAD) to validate that anti-CD31 GNRs were synthesized correctly. Briefly, the surface proteins on anti-CD31 GNRs were separated by sodium dodecyl sulfate-polyacrylamide gel electrophoresis and the gel was stained with Coomassie Brilliant Blue. A digital camera was used to characterize and image the protein components.

2.4. Isolation of human VM-ECs

VM tissues were obtained from clinical patients who underwent resection surgeries of their VMs. This study was approved by the Human Ethics Committee of Shanghai Ninth People's Hospital, Shanghai Jiao Tong University School of Medicine. Informed consents were signed by all patients. After immediately sterilely transported to the central laboratory, the VM tissues were minced and digested for cell isolation. The tissues were scissor minced on ice and digested in 10-cm dishes with 10 mL of Dulbecco's modified Eagle medium (DMEM, Gibco), 1X Ca^{2+}/Mg^{2+} which was dissolved in phosphate-buffered saline solution (PBS, Thermo Fisher), 2% fetal bovine serum (Gibco) and 1 mg/mL of collagenase A (Roche) for 30 min at 37 °C [24]. Next, the digested tissues were homogenized by 5 mL of PBS supplemented with 5% penicillin–streptomycin–glutamine (PSG; Gibco) three times. A 100 μm cell strainer was used for filtering dissociated tissues and the liquid was centrifugated for 6 min at 1500 rpm. The pellet was mixed with endothelial growth medium-2 (EGM-2; CC-3156; Lonza), which was supplemented with 20% FBS and 2% PSG. Then the mixture was cultured onto 10 cm dishes coating with 1 μg/cm^2 of fibronectin (Millipore). Cells were trypsinized with 0.05% trypsin-EDTA (Invitrogen) and centrifugated for 6 min at 1500 rpm when they grew to 80%–90% confluency. Afterward, CD31 positive cells were sorted using anti-CD31 antibody-conjugated magnetic beads (Miltenyi Biotech). These purified VM-ECs were cultured on fibronectin-coated plates at 37 °C, 5% CO_2 supplemented with EGM-2, 20% FBS, and 2% PSG.

2.5. Identification of human VM-ECs, HUVECs and HUSMCs

The VM-ECs were identified by immunofluorescence and western blot. Human umbilical vein endothelial cells (HUVECs) and human uterine smooth muscle cells (HUSMCs) were identified by immunofluorescence staining. For immunofluorescence assay, VM-ECs, HUVECs and HUSMCs were fixed with cold methanol (Fisher Chemicals) at 4 °C for 10 min and blocked in 5% horse serum (Vector Laboratories) in PBS. Anti-CD31 (1:50, Dako), anti-von Willebrand Factor (vWF) (1:100, Dako), anti-VE-Cadherin (1:50, Santa Cruz), anti-α-SMA (1:500, Sigma) and anti-PROX1 (1:50, R&D Systems) were incubated with primary antibody for 1 h followed by FITC which conjugated with secondary antibodies (1:200, Vector Laboratories). Nuclei were detected by DAPI counterstain (ProLong Gold Antifade Reagent with DAPI; Life Technologies).

Fluorescent images were acquired using an immunofluorescence microscope (Nikon). Western blot assays were performed as previously described [24].

2.6. Cell culture, cellular uptake, and cell viability assay

VM-ECs were fed with endothelial cell growth medium (ECGM) (Cell Applications)/10% FBS (HyClone). HUVECs were purchased from Shanghai Institute, Chinese Academy of Sciences and HUSMCs were purchased from ATCC. HUVECs and HUSMCs were cultured in high glucose dulbecco's modified eagle medium (DMEM) supplemented with 10% FBS. TEM assay and 5-FAM fluorescence assay were performed to visualize cell conditions and uptake by coculturing VM-ECs with 80 ppm GNRs, anti-CD31 GNRs, or 5-FAM-*anti*-CD31 GNRs for 2 h or 12 h. After that, part of the cells was treated with an 808 nm NIR laser for 5 min. Finally, both irradiated and unirradiated cells were collected and detected by TEM or an immunofluorescence microscope.

To explore the cytotoxicity and PTT efficiency of anti-CD31 GNRs with or without irradiation, VM-ECs and HUVECs were cultured with different concentrations of anti-CD31 GNRs (0, 20, 40, 80, 120, 160, 320 ppm) for 12 h and a CCK-8 cytotoxicity assay was performed. Briefly, cells were plated in 96-well plates, processed according to the manufacturer's instructions (CCK8 Dojindo CK04-05), and quantified on a Versa Max microplate reader (Molecular Devices). Then VM-ECs co-cultured with 80 ppm GNRs or anti-CD31 GNRs were irradiated by different power densities (0, 0.28, 0.56, 0.84, 1.12 W/cm^2) or different irradiation times (0, 1, 3, 5, 7, 9 min). In another setup, a CCK-8 cell proliferation assay was performed in which the CCK-8 solution was added at day 1, day 3, and day 5 to identify the PTT efficiency of the chosen concentration of anti-CD31 GNRs combined with the appropriate power density on VM-ECs. Part of the treated VM-ECs were cultured for another 12 h to perform a live/dead cell viability assay (Dojindo Laboratories, Shanghai, China). Immunofluorescent pictures were acquired using an immunofluorescence microscope (Nikon).

2.7. Flow cytometry analysis

Flow cytometry was applied for cell apoptosis with Annexin V/PI double staining (BD pharmingen). For the anti-CD31 GNRs group and anti-CD31GNRs + Laser group, the VM-ECs were co-cultured with anti-CD31 GNRs for 12 h when they reached 80%–90% confluency. After incubation, cells were washed with PBS three times. For the anti-CD31 GNRs + Laser group, the VM-ECs were followed by irradiation with 808 nm NIR laser at 0.56 W/cm^2 for 5 min. Next, cells were collected and resuspended in a 100 μl binding buffer. A solution of 5 μl Annexin V-FITC and 5 μl PI were added and the cell suspensions were maintained from light for 15 min. A FACS Calibur flow cytometer (BD Biosciences, USA) was used to detect the fluorescence.

2.8. Western blot analysis

To evaluate the influence of nanorods and NIR laser irradiation on the phenotype of VM-ECs, a Western blot analysis was performed. VM-ECs were divided into 3 groups: the blank control group, the anti-CD31 GNRs group, and the anti-CD31 GNRs + Laser group. VM-ECs cultured in 6-well plates to an 85–90% confluency were harvested and centrifuged. The total cell protein was extracted using the BCA protein assay kit, separated by sodium dodecyl sulfate polyacrylamide gel electrophoresis (SDS-PAGE), and transferred into the polyvinylidene fluoride membrane (Sigma Aldrich, USA). Then skim milk was used to block the membrane and then it can be incubated with the following primary antibodies: rabbit monoclonal anti-cleaved-caspase 3, rabbit monoclonal anti-cleaved-caspase 9, rabbit monoclonal anti-Bax, rabbit polyclonal anti-Bcl-2, rabbit monoclonal anti-Phospho-PI3K (Y458), rabbit monoclonal anti-PI3K, rabbit monoclonal anti-Phospho-AKT (S473), rabbit monoclonal anti-AKT, rabbit monoclonal anti-Ki67, rabbit monoclonal anti-IL-1β, and mouse monoclonal anti-β-actin. Samples were washed with TBST and respective secondary antibodies were incubated for 1 h. Finally, an enhanced chemiluminescence system was utilized to detect the immunoreactive bands.

2.9. Animal model and in vivo PTT

Animal experiments and animal care were performed in accordance with the protocols approved by the Animal Experiment and Care Committee of Shanghai Ninth People's Hospital, Shanghai Jiaotong University School of Medicine. After the cell expansion, HUVECs (2.5–3.5 × 10^5), VM-ECs (2.5–3.5 × 10^5) and HUVECs (2.5–3.5 × 10^5) + HUSMCs (2.5–3.5 × 10^5) were suspended in Matrigel™ (Corning) and injected subcutaneously into one flank of 6-7-week old male athymic nu/nu mice purchased from Shanghai Southern Model Biotechnology Co. Ltd (Shanghai, China). Five days after modeling, 75 μL PBS solution and 75 μL 80 ppm anti-CD31 GNRs were locally injected into12 and 24 mice, respectively. Twelve hours after the injection, an 808 nm NIR laser with a power density of 0.56 W cm^{-2} was used for direct irradiation. Thermal imaging was performed using a FLIR A300 infrared camera with ResearchIR software to record the real-time infrared thermal images and temperature. Part of the lesions were dissected 1, 3, and 5 days after VM xenograft modeling. Other lesions and major organs were dissected 3 days and 7 days after NIR irradiation. The dissected lesions and major organs were fixed in 10% formalin then embedded as paraffin. Hematoxylin and Eosin (H&E) staining was performed in major organs and five images were taken randomly per section using EVOS (Life Technologies).

To further evaluate in vivo biocompatibility of anti-CD31 GNRs including hematology, liver, and kidney functions, blood samples of the mice 7 days after different treatments were collected. By centrifuging the samples for 15 min at 3500 rpm, serum was obtained and stored at 20 °C. Whole blood was stored in EDTA anticoagulant tubes at 4 °C.

2.10. In vivo biodistribution

To study the biodistribution of nanoparticles, VM xenograft mice (n = 3 each group) received a local injection into VM lesions of 75 μL GNRs solution or anti-CD31 GNRs solution at a dose of 5 mg/kg based on Au. Twelve hours after the injection, all mice were euthanized and their hearts, livers, spleens, lungs, kidneys and VMs were dissociated. Organs and VMs were weighed with an electronic scale and Au content of organs or VMs was quantified with ICP-MS.

2.11. Immunohistochemical and immunofluorescence analysis

The immunohistochemical and immunofluorescence staining were adopted to observe the pathological morphology and evaluate the efficacy of PTT as previously described [24]. For immunohistochemical analysis, an anti-CD31 antibody (77,699, Cell Signaling) was used. For immunofluorescence, FITC/Texas Red-conjugated secondary antibody (1:200, Vector Laboratories) was used. Samples were mounted using Prolong Gold with DAPI. A Nikon light microscope (Nikon Corp. Tokyo, Japan) was used for image acquisition. Vascular area quantification was performed by ImageJ software.

2.12. Statistical analysis

All quantitative data were presented as mean ± standard deviation (SD) from three independent experiments. Statistical analyses were performed using GraphPad Prism. The student's t-test or one-way analysis of variance (ANOVA) was performed as appropriate. *P < 0.05, **P < 0.01, and ***P < 0.001.

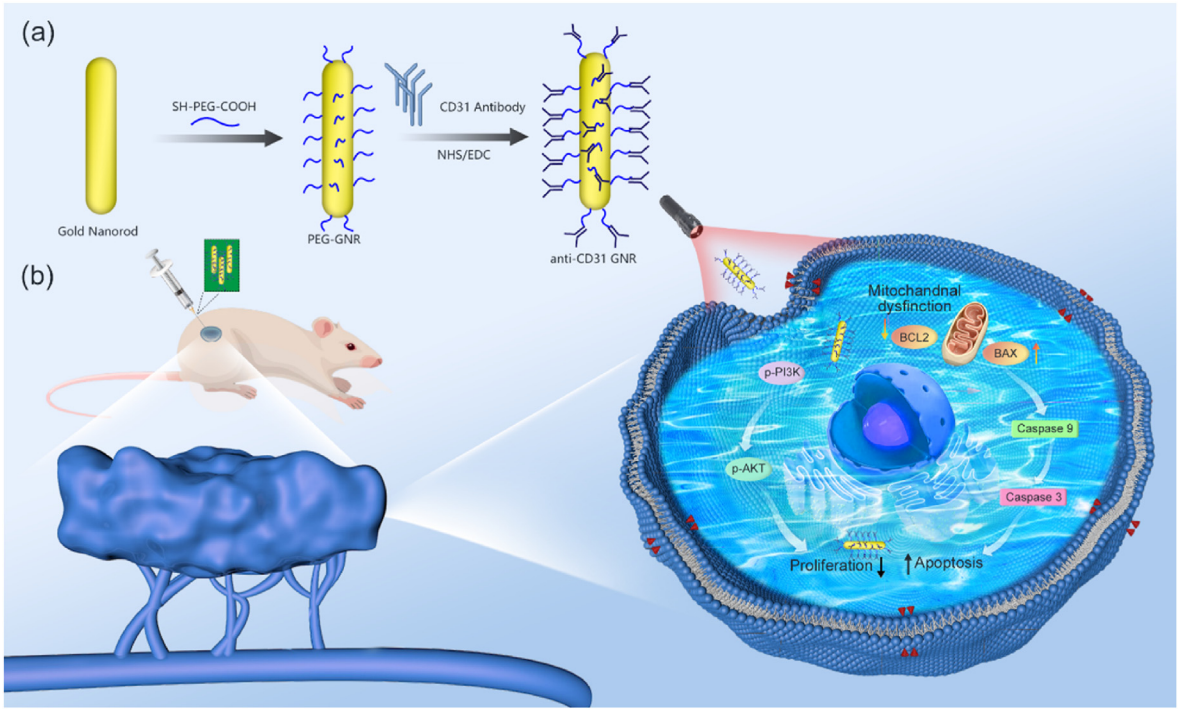

Scheme 1. Schematic design of CD31 antibodies combined with PEG-GNRs for photothermal therapy of venous malformations.

3. Results and discussion

3.1. The synthesis and characterization of GNRs and anti-CD31 GNRs

The synthesis procedure of anti-CD31 GNRs is shown in Scheme 1. GNRs were synthesized and characterized by TEM and UV–vis–NIR. The TEM picture showed GNRs with a size of about 65nm × 15 nm were in good monodispersity (Fig. 1A, Fig. S1). It is considered that 50 nm is appropriate for tumor therapy and 20 nm is suitable for diagnostic tools [29]. Nanorods with small size (<40 nm) have a greater possibility to induce cell damage, while larger nanorods may be quickly metabolized through visceral pathways [30–33]. Therefore, our GNRs may be suitable for photothermal treatment of venous malformations. The UV–vis spectrum revealed that the GNRs had a sharp absorption peak at 840 nm which indicated their strong NIR absorption ability (Fig. 1B).

To achieve better biocompatibility and higher phagocytosis rate, GNRs were modified with PEG chains followed by the binding of CD31 antibodies to the surface of PEG-GNRs which was performed by NHS/EDC chemistry [29]. An absorption band at 1100 cm^{-1}, which is associated with C–*O*–C stretching of PEG, confirms the successful PEGylation of the GNRs (Fig. S2). The final product was analyzed by SDS-PAGE. According to Fig. S3, the product of the anti-CD31 GNRs group had bands which were similar to the CD31 antibody group, indicating that CD31 antibody-modified GNRs were successfully synthesized.

To evaluate the photothermal effect of different concentrations of anti-CD31 GNRs, the temperature evolution under continuous laser irradiation of 808 nm was mapped and quantified by real-time thermal imaging using a thermal camera. As shown in Fig. 1C, D, the nanorod solutions achieved significant increases in solution temperature by 13.3, 19.7, and 26.7 °C following irradiation for 5 min (0.56 W/cm^2) at 20, 40, 80 ppm respectively, while the temperature of the PBS was slightly changed. These results indicated that anti-CD31 GNRs can convert the 808 nm NIR laser energy into heat energy efficiently and rapidly.

3.2. Isolation and characterization of ECs from tissue of VM lesions

VM-ECs were successfully isolated from 3 VM samples, and one primary VM-EC strain with the best growth status was chosen for further experiments. The sorted VM-ECs exhibited the same "cobblestone" morphology as HUVECs (Fig. 2A). Besides, VM-ECs expressed EC-specific cell markers CD31, VE-Cadherin, and vonWillebrand Factor (vWF) but no lymphatic marker Prox1 or smooth muscle marker α-SMA. On the contrary, HUSMCs expressed smooth muscle marker α-SMA which was shown in Fig. S4. The western blot analysis revealed a significant phosphorylation activation of TIE2 protein (Fig. 2B C) and aberrant activation of PI3K/AKT pathway in the VM-EC population compared to HUVECs, indicating a representative strain was isolated from sporadic VMs (Fig. S5). These results verified the purified VM-ECs cell line was successfully established.

3.3. Construction of VM-EC xenograft model in nude mice

Venous malformations are congenital developmental malformations, which are characterized by a single layer of endothelial cells forming anomalous blood vessels surrounded by disorganized smooth muscle cells and pericytes [34,35]. By now, a few animal models have been constructed for different applications. Castel used $PIK3CA^{Sprr2f-Cre}$ mice to develop spinal and cutaneous VMs [22]. Boscolo and Goines generated xenograft VM models by injecting the mixture of HUVEC-TIE2-L914F or VM-ECs with Matrigel subcutaneously into immune-deficient mice [5, 24]. Using HUVEC mutated cell line can obtain quickly enlarged VM lesions and stable modeling procedures. However, there are differences in cellular activities between HUVECs and VM-ECs which may not be represented in HUVEC-TIE2-L914F model. Using primary VM-ECs can protect the integrity of genetic materials and achieve a similar physiological environment in vivo. Different from tumor cells, VM-ECs are not highly proliferative or invasive cells and a subcutaneous transplantation environment may be not suitable for the early survival and the growth of VM-ECs after transplantation, though matrigel promotes proliferation and tube formation to some extent [21]. Therefore, we aimed to provide a modified method that can accelerate the speed of enlargement of VM lesions while remain the integrity of genetic materials by using primary VM-ECs. We mixed VM-ECs and HUSMCs at a ratio of 1:1 and resuspended in Matrigel (Fig. 3). This modified model has early appearance of

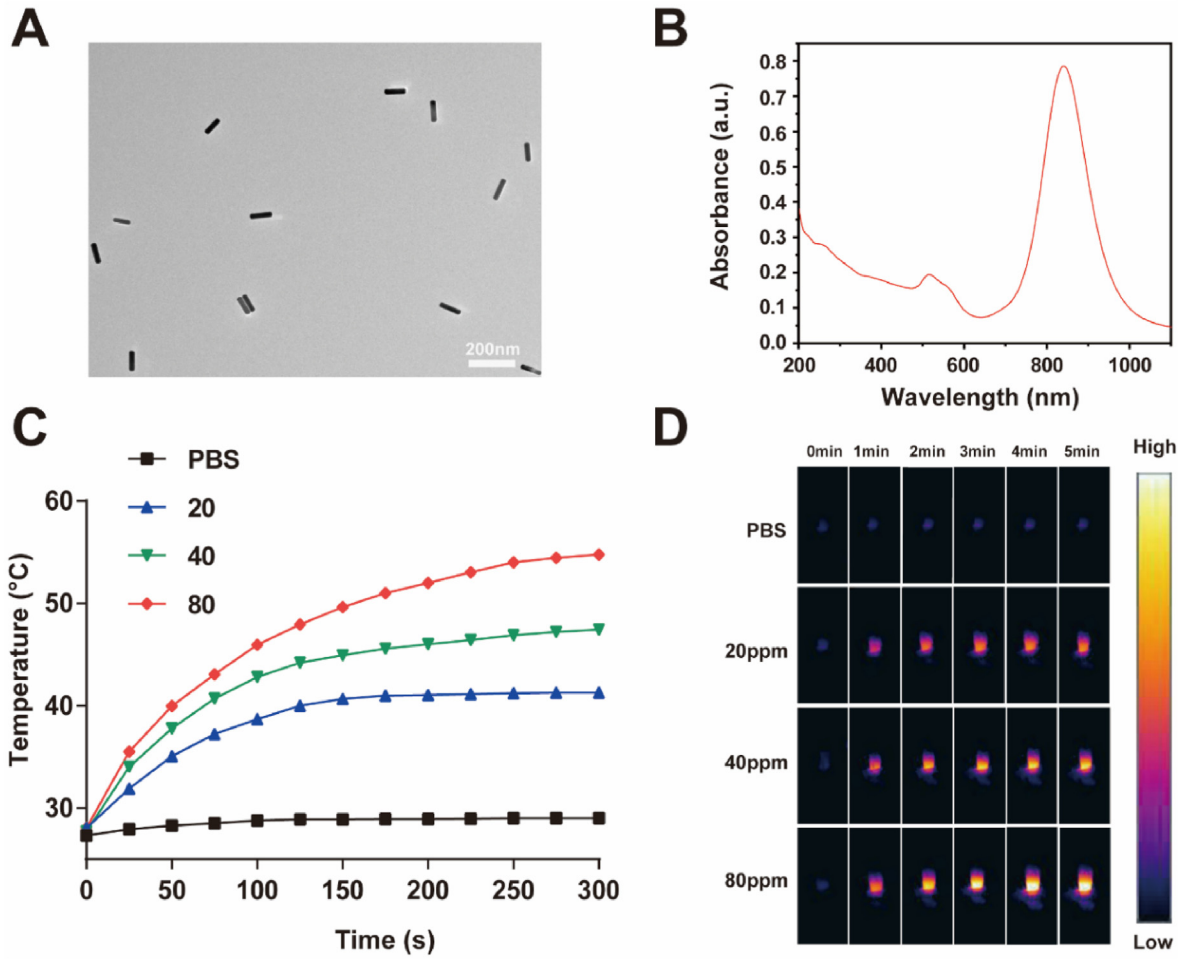

Fig. 1. Synthesis and characterization of the GNRs and anti-CD31 GNRs. (A) TEM image of GNRs. (B) UV–vis spectrum of the GNRs' solution. (C) Photothermal effect of different concentrations of the anti-CD31 GNRs (0, 20, 40, 80 ppm) illuminated with 808 nm NIR laser (0.56 W cm^{-2}). (D) Temperature profile of various groups after being irradiated with 808 nm NIR laser for 5 min.

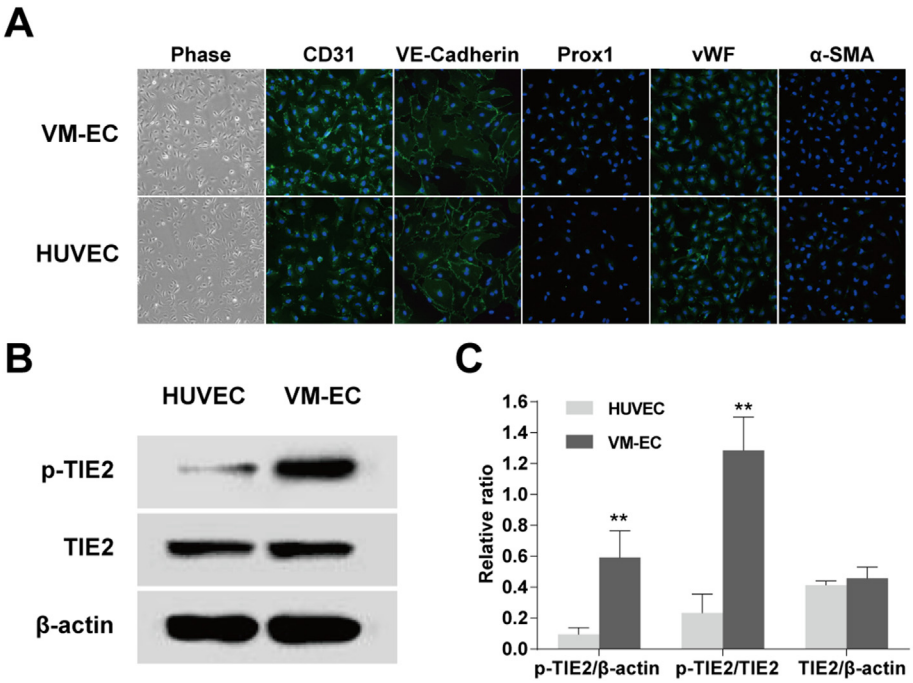

Fig. 2. Characterization of VM-ECs and relative marker expression (A) VM-ECs and HUVECs stained positive for endothelial markers CD31, VE-Cadherin and vWF while negative for smooth muscle marker α-SMA and lymphatic marker Prox1. (B, C) Western Blot analysis of TIE2 activation difference between VM-ECs and HUVECs which indicated an elevation of phosphorylation TIE2 in VM-ECs. β-actin served as a loading control. The one-way analysis of variance was performed to compare data between groups. *P < 0.05; **P < 0.01.

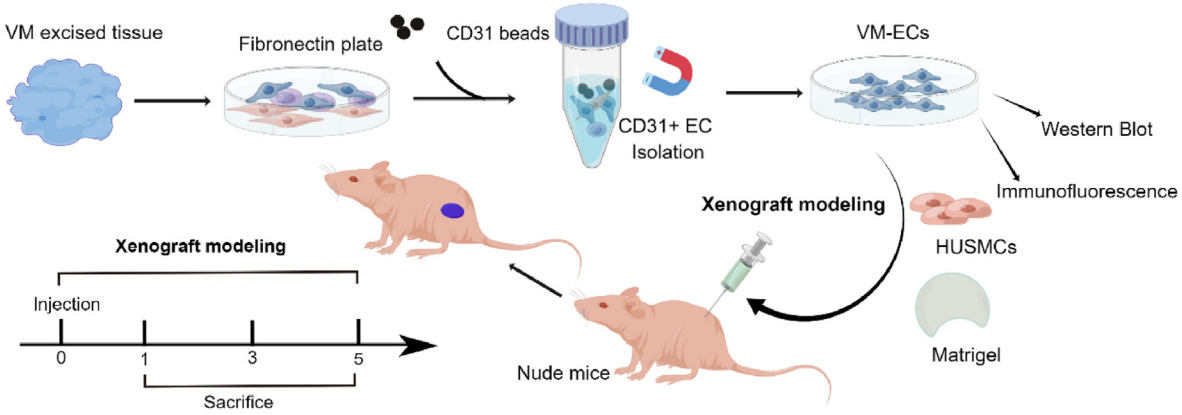

Fig. 3. Schematic of VM xenograft modeling approach (drawn by Figdraw).

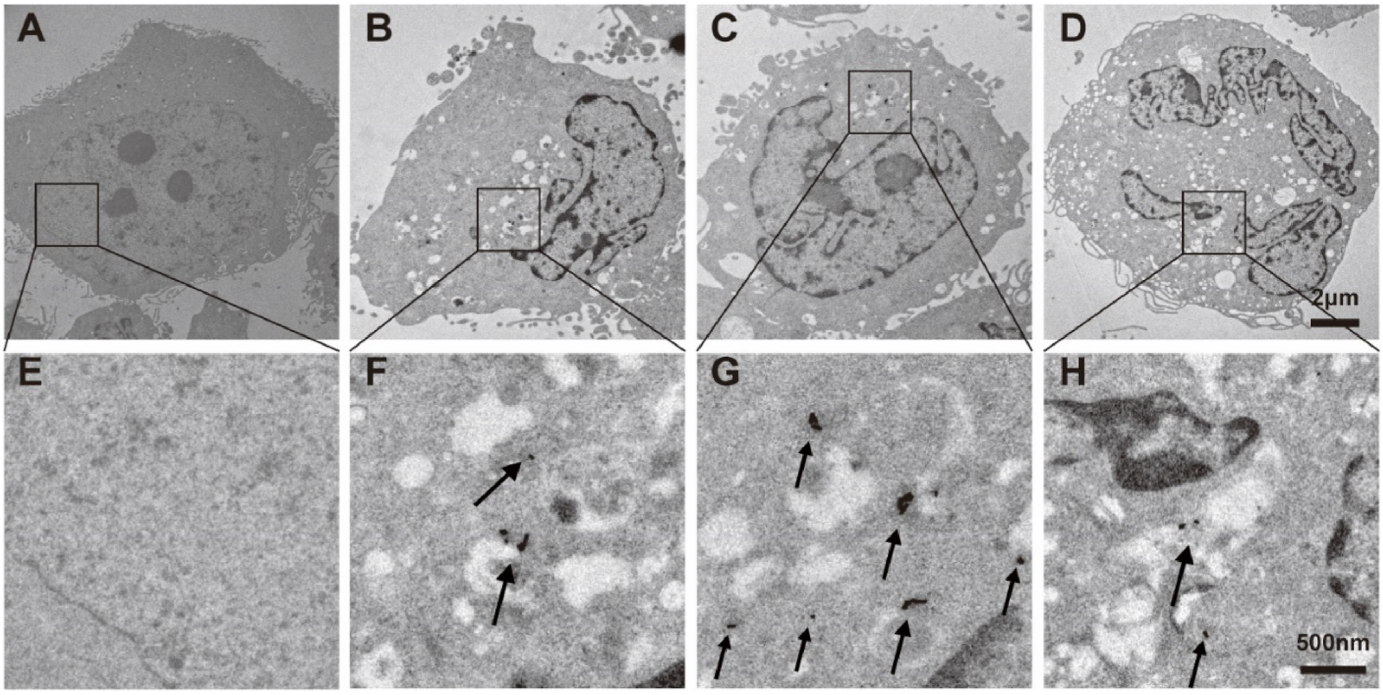

Fig. 4. Representative TEM images of VM-ECs with or without anti-CD31 GNRs and laser irradiation. (A) Normal VM-ECs without anti-CD31 GNRs. (B) VM-ECs co-incubated with 80 ppm GNRs and no significant organelle injuries were observed. However, only a small amount of GNRs were phagocytosed by the VM-ECs. (C) VM-ECs co-incubated with 80 ppm anti-CD31 GNRs demonstrated more significant phagocytosis of the nanoparticles and no organelle injuries were observed. (D) After 12 h of coculturing with 80 ppm anti-CD31 GNRs and exposure to an 808 nm NIR laser at a power density of 0.56 W cm^{-2} for 5 min, VM-ECs showed some nucleus karyotheca were dissolved and broken, and some remaining anti-CD31 GNRs were internalized in the cytoplasm of the cell. (E) High magnification of image (A). (F) High magnification of image (B). (G) High magnification of image (C). (H) High magnification of image (D).

pathological structures similar to human VMs, such as wide deformed venous lumens and loose endothelial structures (Fig. S6). This may be because the interaction between HUSMC and VM-ECs creates a pathological environment that is more in line with the survival of VM-ECs.

3.4. Cellular uptake of anti-CD31 GNRs

Before determining the cytotoxicity and photothermal properties of anti-CD31 GNRs on VM-ECs, we explored the phagocytosis of VM-ECs by 5-FAM fluorescence assay and TEM. As shown in Fig. S7, VM-ECs could gradually take up 5-FAM-*anti*-CD31 GNRs. Fig. 4A and E are normal VM-ECs while Fig. 4B, C, D, F, G, and H are VM-ECs co-incubated with anti-CD31 GNRs. After 12 h of coculture with 80 ppm anti-CD31 GNRs, VM-ECs engulfed several nanorods and no significant organelle injures were observed. While cells demonstrated significant nuclear lysis after being exposed to 808 nm NIR laser for 5 min. The TEM assay indicated that PTT combined with anti-CD31 GNRs could trigger significant death of VM-ECs.

3.5. In vitro photothermal therapy

The cytotoxicity of anti-CD31 GNRs was reflected by the relative viability of cells with different concentrations. As shown in Fig. 5A, no adverse effect was observed in both HUVECs and VM-ECs with the concentration of 80 ppm while both kinds of cells demonstrated a significant decrease in cell viabilities with a concentration of ≥120 ppm. Therefore, anti-CD31 GNRs with a concentration of 80 ppm was selected as the appropriate condition for co-incubation with VM-ECs in subsequent experiments. Next, the effects of a certain concentration of nanorods with different NIR laser power densities on VM-ECs were evaluated. With the

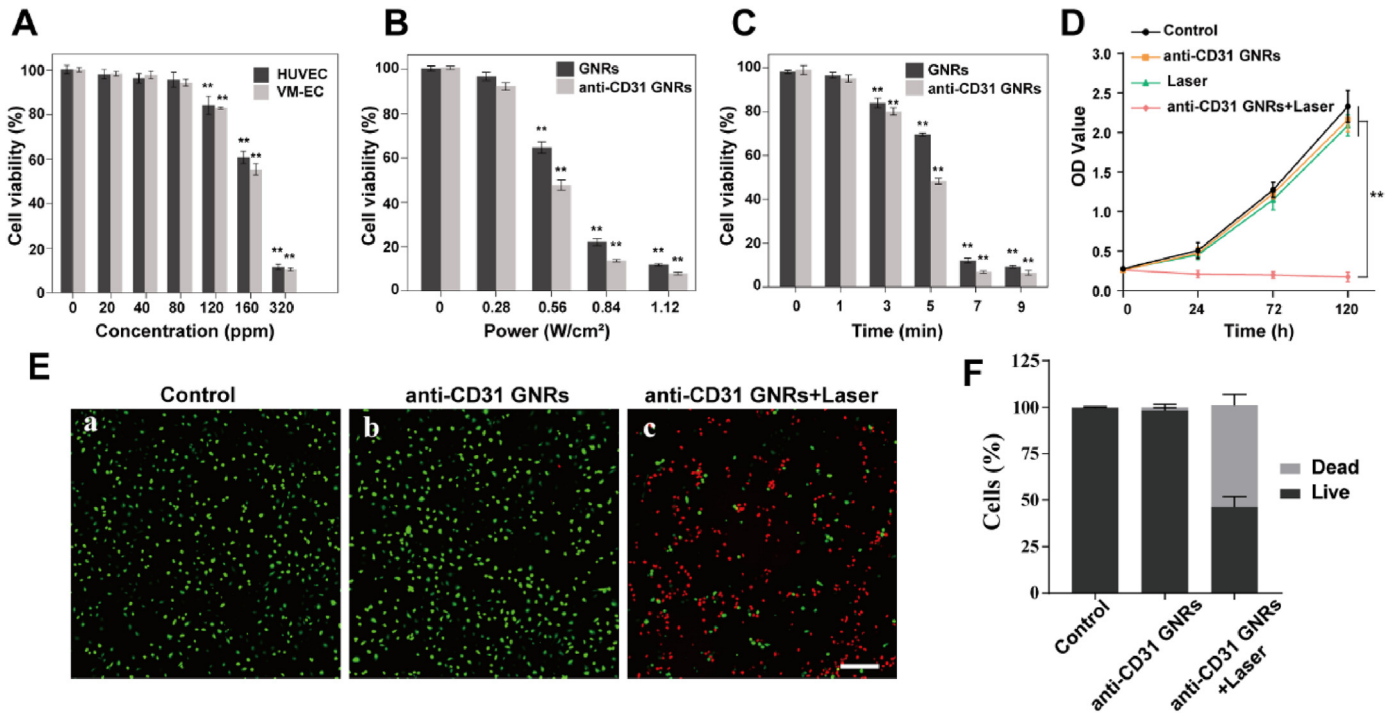

Fig. 5. Assessment of in vitro photothermal therapy. (A) Cytotoxicity of anti-CD31 GNRs on HUVECs and VM-ECs. (B) Cytotoxicity of VM-ECs co-incubated with 80 ppm GNRs or anti-CD31 GNRs and treated with different NIR power densities for 5 min. (C) Cytotoxicity of VM-ECs co-incubated with 80 ppm GNRs or anti-CD31 GNRs and treated with 808 nm NIR laser (0.56 W cm^{-2}) for different time durations. (D) The cell proliferation assay to identify the PTT efficiency of the concentration of 80 ppm anti-CD31 GNRs combined with the power density of 0.56 W/cm^2 on VM-ECs. (E, F) Representative images of Calcein AM (green)/PI (red) staining after incubation with the anti-CD31 GNRs with or without NIR laser irradiation (808 nm, 0.56 W cm^{-2}). The green and red areas represent the regions of living and dead cells, respectively. Values are expressed as mean ± SD. *p < 0.05, **p < 0.01. (n = 3). All scale bars are 200 μm.

increase of laser power densities, the viability of VM-ECs progressively decreased and 0.56 W/cm^2 was proved to be an appropriate laser power density with approximate cell viability of 50% (Fig. 5B). The influence of NIR irradiation time was then analyzed indicating 5 min of irradiation contributed to proper therapeutic effect (Fig. 5C). Furthermore, we performed a cell proliferation experiment lasting for 5 days. As shown in Fig. 5D, the viability of VM-ECs in the anti-CD31GNRs + Laser group was markedly inhibited in 24 h and showed no increase in the following 5 days. The photothermal effect was also detected visibly by using the LIVE/DEAD cell staining (Fig. 5E and F). As shown in Fig. 5F, the viabilities were 99.64% ± 0.36%, 98.27% ± 1.63%, and 47.05% ± 7.05% in groups of control, anti-CD31GNRs, anti-CD31GNRs + Laser respectively. These results verified the satisfactory therapeutical effect of PTT in vitro. However, the underlying treatment mechanisms needed to be clarified.

Gold nanoparticles are particularly effective in damaging tumor cells via several pathways, including stimulation of pro-apoptotic protein expression, inhibition of tumor cells migration, and suppression of epithelial-to-mesenchymal transition [36–38]. The process of necrosis has the potential to amplify tissue inflammation and contribute to severe tissue damage while apoptosis is a preferred mode of cell death avoiding collateral damage and inflammation. However, whether the photothermal effect of anti-CD31 GNRs triggered VM-ECs death via necrosis or apoptosis was still unclear. To definitively address this issue, the treated cells were analyzed by flow cytometry and Western Blot assays. Flow cytometric analysis of cell apoptosis showed that the percentage of VM-ECs apoptosis for group anti-CD31 GNRs + Laser was significantly lower than the anti-CD31 GNRs group and control group (Fig. 6A). Western Blot assays showed that the mitochondrial apoptosis pathway was activated (Fig. 6B and C). Moreover, to discover other underlying mechanisms of the therapy, we tested other proteins, including Ki-67 for cell proliferation, IL-1β for inflammation, and the well-known PI3K/AKT pathway (Fig. 6D and E). We found a significantly lower expression of Ki-67, IL-1β and TNF-α in the anti-CD31 GNRs + Laser group which indicated the therapy could effectively inhibit the proliferation of VM-ECs and avoid strong inflammatory responses. Aberrant signal transduction in the PI3K/AKT pathway is one of the major pathogenic factors of venous malformations [5,21]. Studies have proved that mutations in TIE2 can increase TIE2 autophosphorylation level and result in aberrant activation of PI3K/AKT pathway, followed by vascular morphogenesis, and finally lead to venous malformations. Phosphorylation of PI3K and AKT indicated the activation of this signal pathway. In the present experiments, the phosphorylated PI3K and AKT expression of VM-ECs cocultured with anti-CD31 GNRs were significantly decreased after photothermal irradiation. In the other two groups, aberrant activation of the signal pathway still existed. To conclude, the therapeutic effect may be the result of both the activation of the mitochondrial apoptosis pathway and the inhibition of the PI3K/AKT pathway.

3.6. *In vivo therapeutic efficacy of PTT*

A modified xenograft VM mouse model was constructed to investigate the therapeutic effect of anti-CD31 GNRs with laser irradiation. A solution of 80 ppm anti-CD31 GNRs (75 μL) or PBS was injected into xenograft site locally. After 12 h of the injection, one of the experiment group and PBS group were chosen to receive local irradiation (0.56 W cm^{-2}) by using an 808 nm NIR laser for 5 min. In vivo photothermal imaging of VM xenograft nude mice after different treatments (PBS + Laser or anti-CD31 GNRs + Laser) were recorded (Fig. 7A and B). As the figure presented, the injection of anti-CD31 GNRs accompanied with laser irradiation led to significant thermal contrast, with the highest temperature reached to 46.3 °C, indicating the optimal condition among groups. In contrast, the temperature in the VM xenograft site only increased by 4.9 °C after being treated with PBS under 808-nm laser irradiation for 5 min.

Three days and seven days after laser irradiation, the VM xenograft samples were collected from sacrificed mice and prepared into paraffin sections. Then the immunofluorescence and immunohistochemistry

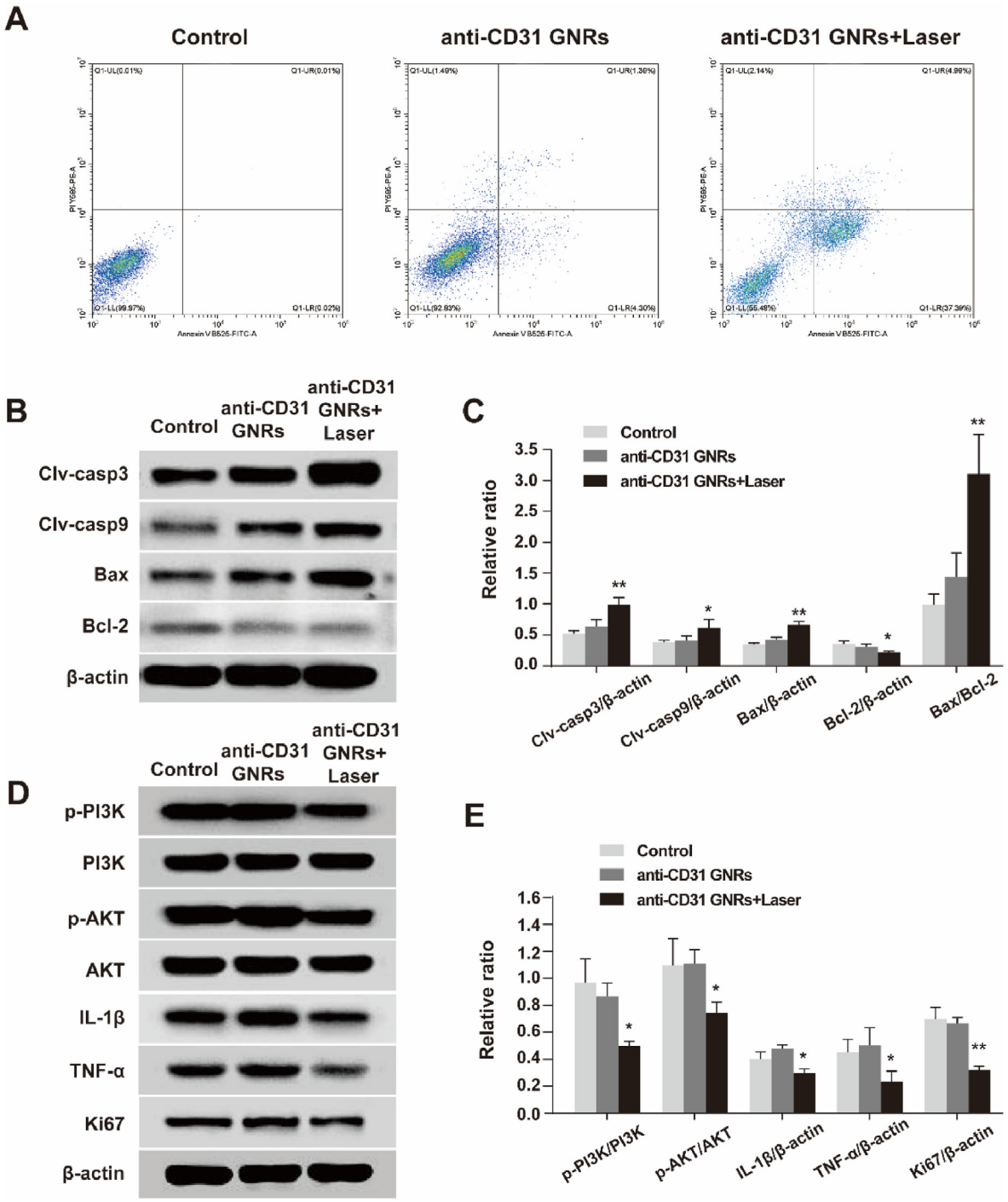

Fig. 6. Anti-CD31 GNRs-based PTT induced apoptosis and proliferation suppression in vitro. (A) Flow cytometric analysis of cell apoptosis of VM-ECs after incubation with anti-CD31 GNRs treated with or without PTT. (B, C) Western blot analysis of apoptosis-related proteins in VM-ECs treated with or without laser irradiation. (D, E) Western blot analysis of the proliferation, inflammation, and PI3K/AKT signaling pathway-related proteins in VM–ECs treated with or without laser irradiation. The β-actin protein level was used as a control. ($n \geq 3$, *$P < 0.05$, **$P < 0.01$).

staining were performed. VM sections were profiled by immunofluorescence microscopy for CD31 and α-SMA expression which are ECs-specific and SMCs-specific markers, respectively. As shown in Fig. 7C and F, in the control group and anti-CD31 GNRs group, typical VM lesions were observed which are characterized by ectatic EC-lined channels covered by rare and abnormally distributed SMCs. The numbers of VM-ECs were counted on day3 and day7 (Fig. 7D, G). The anti-CD31 GNRs + Laser group showed significantly fewer VM-ECs and smaller lumens or disorganized vessel structures were observed either (Fig. 7E, H). Immunofluorescence analysis showed that the vessel area of the anti-CD31 GNRs + Laser group was only approximately 25% on day 3 and 12% on day 7 compared to the control group and no typical enlarged channel was observed on day 7 (Fig. 7E, H). These results demonstrated the effectiveness of PTT with anti-CD31 GNRs for the treatment of VM in vivo.

Furthermore, GNRs and anti-CD31 GNRs were locally injected into VM lesions and tissue uptake of the nanorods was measured in terms of Au content through ICP-MS. The results demonstrated that the Au

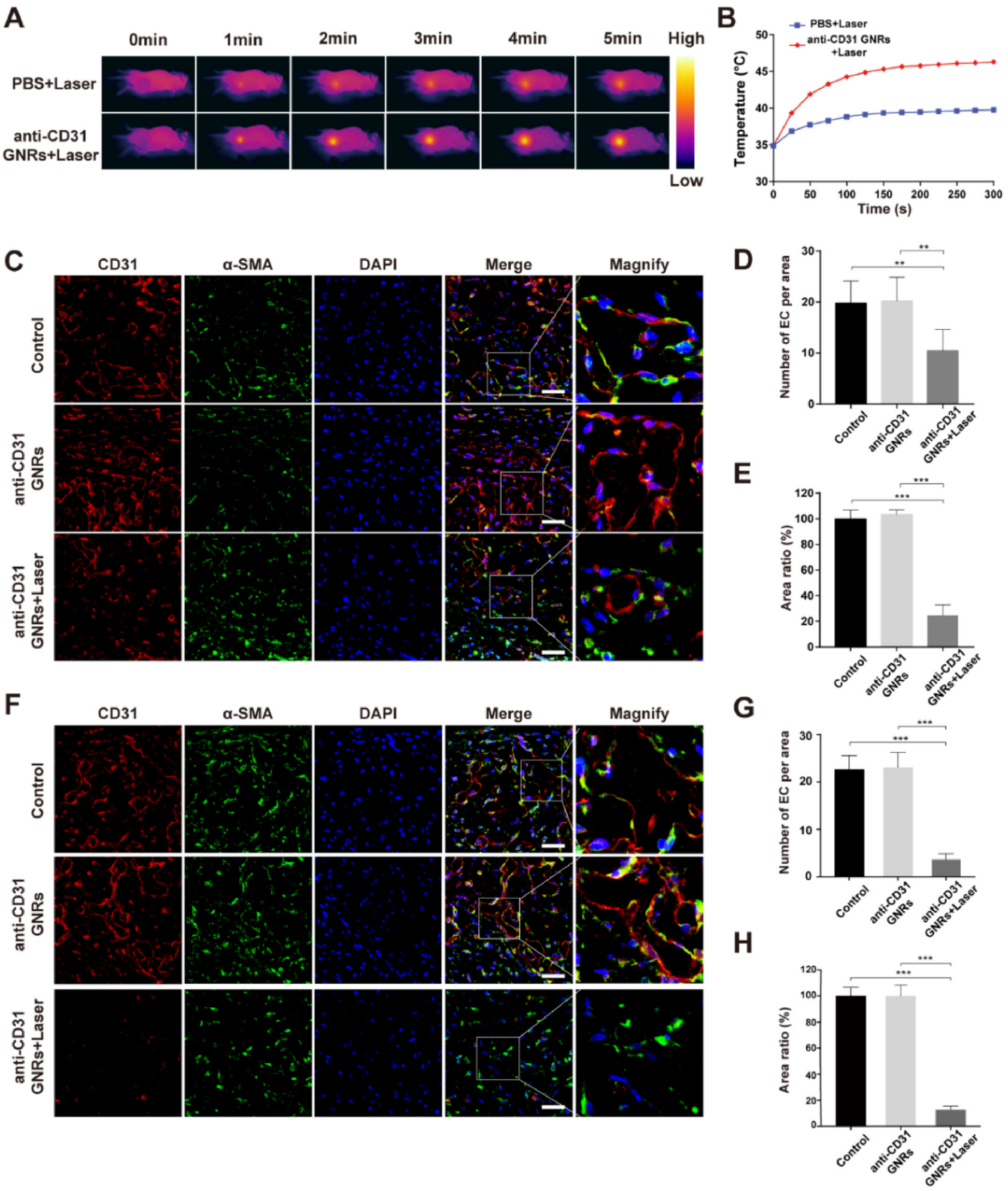

Fig. 7. Anti-CD31 GNRs-based PTT eliminated VM lesions in vivo. (A, B) In vivo thermal images and temperature changes of VM xenograft mice after different treatments when exposed to an 808 nm laser at 0.56 W/cm^2 for 5 min. (C) Treatment effect of NIR irradiation. Immunofluorescence staining of CD31, α-SMA, and DAPI after 3 days. (D) Statistical analysis of VM-ECs per area 3 days after different treatments. (E) Statistical analysis of relative luminal area 3 days after different treatments. (F) Treatment effect of NIR irradiation. Immunofluorescence staining of CD31, α-SMA, and DAPI after 7 days. (G) Statistical analysis of VM-ECs per area 7 days after different treatments. (H) Statistical analysis of relative luminal area 7 days after different treatments. Scale bars = 50 μm *P < 0.05, **P < 0.01, ***P < 0.001.

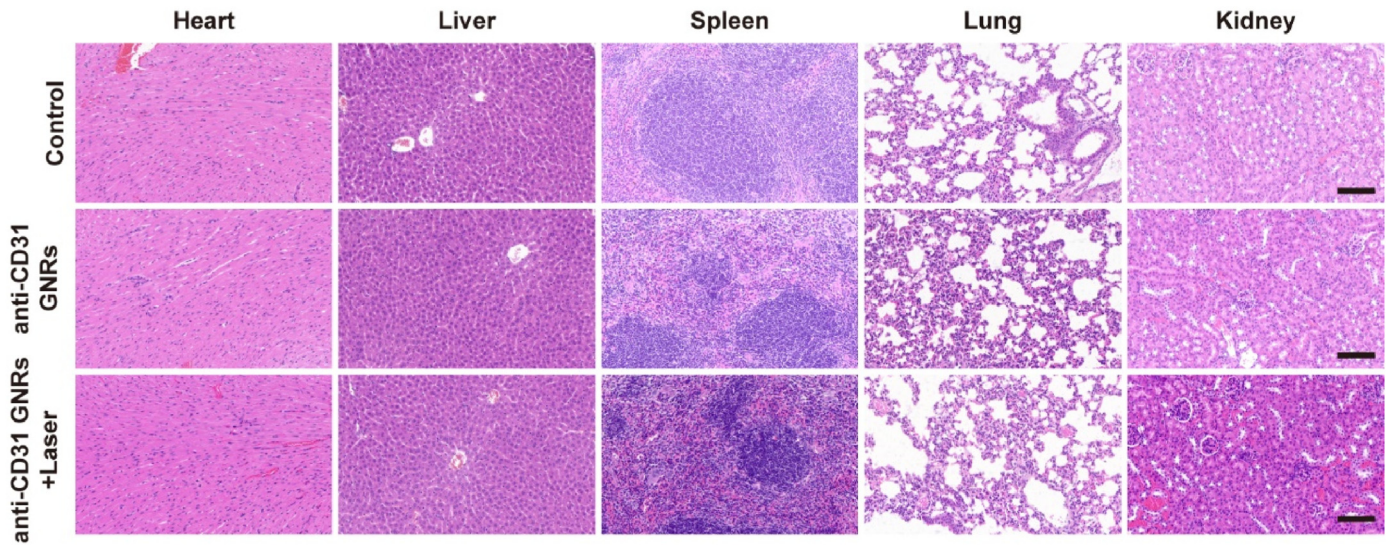

Fig. 8. H&E staining of slices of the heart, liver, spleen, lung, and kidney from xenograft nude mice after different treatments for 7 days. All of the organs appear histologically normal. Scale bars = 100 μm.

content of VM xenograft lesion in anti-CD31 GNRs group was significantly higher than GNRs group (Fig. S8).

3.7. In vivo biocompatibility

To evaluate the biocompatibility, mice were sacrificed 3 days and 7 days after PTT treatment. HE staining of major organs was performed, including heart, liver, spleen, lung, and kidney (Fig. S9 and Fig. 8). No obvious tissue damage was found in comparison with the control group. Besides, there was no obvious difference in the hematology, liver, and kidney functions among these groups (Fig. S10). The phenomenon indicated that the application of anti-CD31 GNRs-based PTT in VM treatment was safe and feasible.

4. Conclusion

In the present study, we successfully synthesized non-toxic and good biocompatible anti-CD31 GNRs which could be applied specifically to treat venous malformations. In vitro experiments demonstrated effective ablation of PTT at specific conditions on VM-ECs. For in vivo experiments, we modified a VM xenograft model and confirmed that an injection of anti-CD31 GNRs followed by 808 nm NIR laser significantly reduced VM-EC number and lumen area. Potential mechanisms were explored but remain speculative. Further studies could focus on parameter adjustment to improve therapeutic effects, specific mechanisms of the PTT on VM, and multiple applications for this VM xenograft model. In conclusion, our study has proved that anti-CD31 GNRs with 808 nm NIR laser is a promising strategy for VM treatment.

Data and materials availability

All data are available on request.

Credit author statement

Yihong Jiang: Conceptualization, Methodology, Investigation, Validation, Formal analysis, Resources, Writing – original draft. **Junchao Liu**: Methodology, Validation, Formal analysis, Writing – review & editing. **Jinbao Qin**: Methodology, Validation, Writing – review & editing. **Jiahao Lei**: Methodology, Validation, Writing – review & editing. **Xing Zhang**: Conceptualization, Methodology, Formal analysis, Writing – review & editing. **Zhijue Xu**: Methodology, Writing – review & editing. **Weimin Li**: Formal analysis, Writing – review & editing. **Xiaobing Liu**: Methodology, Writing – review & editing. **Ruihua Wang**: Methodology, Formal analysis, Writing – review & editing. **Bo Li**: Funding acquisition, Methodology, Supervision, Writing – review & editing. **Xinwu Lu**: Funding acquisition, Conceptualization, Methodology, Validation, Formal analysis, Supervision, Resources, Writing – review & editing.

Declaration of competing interest

The authors declare that they have no known competing financial interests or personal relationships that could have appeared to influence the work reported in this paper.

Acknowledgment

Y. H. Jiang, J. C. Liu, J. B. Qin, J. H. Lei contributed equally to the work. The authors thank Prof. Zhihong Nie (Fudan University) for the synthesis and characterization of gold nanorods. This work was partially funded by the National Natural Science Foundation of China (82170509, 51890892, 82170488, 81971712 and 82170411), Natural Science Foundation of Shanghai (20ZR1431400), Shanghai Sailing Program (20YF1423800), and Fundamental research program funding of Ninth People's Hospital affiliated to Shanghai Jiao Tong University School of Medicine (JYZZ142).

Appendix A. Supplementary data

Supplementary data to this article can be found online at https://doi.org/10.1016/j.mtbio.2022.100401.

References

[1] M. Vikkula, L.M. Boon, J.B. Mulliken, Molecular genetics of vascular malformations, Matrix Biol. 20 (2001) 327–335, https://doi.org/10.1016/S0945-053X(01)00150-0.
[2] S. Eifert, J.L. Villavicencio, T.-C. Kao, B.M. Taute, N.M. Rich, Prevalence of deep venous anomalies in congenital vascular malformations of venous predominance, J. Vasc. Surg. 31 (2000) 462–471, https://doi.org/10.1067/mva.2000.101464.
[3] S. Behravesh, W. Yakes, N. Gupta, S. Naidu, B.W. Chong, A. Khademhosseini, R. Oklu, Venous malformations: clinical diagnosis and treatment, Cardiovasc. Diagn. Ther. 6 (2016) 557, https://doi.org/10.21037/cdt.2016.11.10.
[4] A.M. Hammill, M. Wentzel, A. Gupta, S. Nelson, A. Lucky, R. Elluru, R. Dasgupta, R.G. Azizkhan, D.M. Adams, Sirolimus for the treatment of complicated vascular

anomalies in children, Pediatr. Blood Cancer 57 (2011) 1018–1024, https://doi.org/10.1002/pbc.23124.
[5] E. Boscolo, N. Limaye, L. Huang, K.-T. Kang, J. Soblet, M. Uebelhoer, A. Mendola, M. Natynki, E. Seront, S. Dupont, Rapamycin improves TIE2-mutated venous malformation in murine model and human subjects, J. Clin. Invest. 125 (2015) 3491–3504, https://doi.org/10.1172/JCI76004.
[6] D.M. Adams, C.C. Trenor, A.M. Hammill, A.A. Vinks, M.N. Patel, G. Chaudry, M.S. Wentzel, P.S. Mobberley-Schuman, L.M. Campbell, C. Brookbank, Efficacy and safety of sirolimus in the treatment of complicated vascular anomalies, Pediatrics 137 (2016), https://doi.org/10.1542/peds.2015-3257.
[7] J.M. Mack, B. Verkamp, G.T. Richter, R. Nicholas, K. Stewart, S.E. Crary, Effect of sirolimus on coagulopathy of slow-flow vascular malformations, Pediatr. Blood Cancer 66 (2019), e27896, https://doi.org/10.1002/pbc.27896.
[8] Y. Chen, Y. Gao, Y. Chen, L. Liu, A. Mo, Q. Peng, Nanomaterials-based photothermal therapy and its potentials in antibacterial treatment, J. Contr. Release 328 (2020) 251–262, https://doi.org/10.1016/j.jconrel.2020.08.055.
[9] N. Fernandes, C.F. Rodrigues, A.F. Moreira, I.J. Correia, Overview of the application of inorganic nanomaterials in cancer photothermal therapy, Biomater. Sci. 8 (2020) 2990–3020, https://doi.org/10.1039/D0BM00222D.
[10] Z.M. Markovic, L.M. Harhaji-Trajkovic, B.M. Todorovic-Markovic, D.P. Kepić, K.M. Arsikin, S.P. Jovanović, A.C. Pantovic, M.D. Dramićanin, V.S. Trajkovic, In vitro comparison of the photothermal anticancer activity of graphene nanoparticles and carbon nanotubes, Biomaterials 32 (2011) 1121–1129, https://doi.org/10.1016/j.biomaterials.2010.10.030.
[11] M. Hao, C. Kong, C. Jiang, R. Hou, X. Zhao, J. Li, Y. Wang, Y. Gao, H. Zhang, B. Yang, Polydopamine-coated Au-Ag nanoparticle-guided photothermal colorectal cancer therapy through multiple cell death pathways, Acta Biomater. 83 (2019) 414–424, https://doi.org/10.1016/j.actbio.2018.10.032.
[12] J. Nam, S. Son, L.J. Ochyl, R. Kuai, A. Schwendeman, J.J. Moon, Chemo-photothermal therapy combination elicits anti-tumor immunity against advanced metastatic cancer, Nat. Commun. 9 (2018) 1–13, https://doi.org/10.1038/s41467-018-03473-9.
[13] S. Pal, A. Ray, C. Andreou, Y. Zhou, T. Rakshit, M. Wlodarczyk, M. Maeda, R. Toledo-Crow, N. Berisha, J. Yang, DNA-enabled rational design of fluorescence-Raman bimodal nanoprobes for cancer imaging and therapy, Nat. Commun. 10 (2019) 1–13, https://doi.org/10.1038/s41467-019-09173-2.
[14] X. Yi, H. Zhou, Y. Chao, S. Xiong, J. Zhong, Z. Chai, K. Yang, Z. Liu, Bacteria-triggered tumor-specific thrombosis to enable potent photothermal immunotherapy of cancer, Sci. Adv. 6 (2020), https://doi.org/10.1126/sciadv.aba3546 eaba3546.
[15] J. Qin, Z. Peng, B. Li, K. Ye, Y. Zhang, F. Yuan, X. Yang, L. Huang, J. Hu, X. Lu, Gold nanorods as a theranostic platform for in vitro and in vivo imaging and photothermal therapy of inflammatory macrophages, Nanoscale 7 (2015) 13991–14001, https://doi.org/10.1039/C5NR02521D.
[16] X. Zhang, J. Liu, X. Yang, G. He, B. Li, J. Qin, P.R. Shearing, D.J. Brett, J. Hu, X. Lu, CuCo 2 S 4 nanocrystals as a nanoplatform for photothermal therapy of arterial inflammation, Nanoscale 11 (2019) 9733–9742, https://doi.org/10.1039/C9NR00772E.
[17] F. Jabeen, M. Najam-ul-Haq, R. Javeed, C.W. Huck, G.K. Bonn, Au-nanomaterials as a superior choice for near-infrared photothermal therapy, Molecules 19 (2014) 20580–20593, https://doi.org/10.3390/molecules191220580.
[18] M.R. Ali, M.A. Rahman, Y. Wu, T. Han, X. Peng, M.A. Mackey, D. Wang, H.J. Shin, Z.G. Chen, H. Xiao, Efficacy, long-term toxicity, and mechanistic studies of gold nanorods photothermal therapy of cancer in xenograft mice, Proc. Natl. Acad. Sci. USA 114 (2017) E3110–E3118, https://doi.org/10.1073/pnas.1619302114.
[19] L. Fan, W. Wang, Z. Wang, M. Zhao, Gold nanoparticles enhance antibody effect through direct cancer cell cytotoxicity by differential regulation of phagocytosis, Nat. Commun. 12 (2021) 1–13, https://doi.org/10.1038/s41467-021-26694-x.
[20] Z. Miao, Z. Gao, R. Chen, X. Yu, Z. Su, G. Wei, Surface-bioengineered gold nanoparticles for biomedical applications, Curr. Med. Chem. 25 (2018) 1920–1944, https://doi.org/10.2174/0929867325666180117111404.
[21] N. Limaye, V. Wouters, M. Uebelhoer, M. Tuominen, R. Wirkkala, J.B. Mulliken, L. Eklund, L.M. Boon, M. Vikkula, Somatic mutations in angiopoietin receptor gene TEK cause solitary and multiple sporadic venous malformations, Nat. Genet. 41 (2009) 118–124, https://doi.org/10.1038/ng.272.
[22] P. Castel, F.J. Carmona, J. Grego-Bessa, M.F. Berger, A. Viale, K.V. Anderson, S. Bague, M. Scaltriti, C.R. Antonescu, E. Baselga, Somatic PIK3CA mutations as a driver of sporadic venous malformations, Sci. Transl. Med. 8 (2016), https://doi.org/10.1126/scitranslmed.aaf1164, 332ra42-332ra42.
[23] G. Chen, J.-G. Ren, W. Zhang, Y.-F. Sun, F.-Q. Wang, R.-F. Li, J. Zhang, Y.-F. Zhao, Disorganized vascular structures in sporadic venous malformations: a possible correlation with balancing effect between Tie2 and TGF-β, Sci. Rep. 4 (2014) 1–9, https://doi.org/10.1038/srep05457.
[24] J. Goines, X. Li, Y. Cai, P. Mobberley-Schuman, M. Metcalf, S.J. Fishman, D.M. Adams, A.M. Hammill, E. Boscolo, A xenograft model for venous malformation, Angiogenesis 21 (2018) 725–735, https://doi.org/10.1007/s10456-018-9624-7.
[25] B. Nikoobakht, M.A. El-Sayed, Preparation and growth mechanism of gold nanorods (NRs) using seed-mediated growth method, Chem. Mater. 15 (2003) 1957–1962, https://doi.org/10.1021/cm020732l.
[26] M.G. da Silva, A.M. Nunes, S.M. Meneghetti, M.R. Meneghetti, New aspects of gold nanorod formation via seed-mediated method, Compt. Rendus Chem. 16 (2013) 640–650, https://doi.org/10.1016/j.crci.2013.01.013.
[27] S. Centi, F. Tatini, F. Ratto, A. Gnerucci, R. Mercatelli, G. Romano, I. Landini, S. Nobili, A. Ravalli, G. Marrazza, In vitro assessment of antibody-conjugated gold nanorods for systemic injections, J. Nanobiotechnol. 12 (2014) 1–10, https://doi.org/10.1186/s12951-014-0055-3.
[28] K. Nam, T. Kimura, A. Kishida, Controlling coupling reaction of EDC and NHS for preparation of collagen gels using ethanol/water co-solvents, Macromol. Biosci. 8 (2008) 32–37, https://doi.org/10.1002/mabi.200700206.
[29] M. Mioc, I.Z. Pavel, R. Ghiulai, D.E. Coricovac, C. Farcaș, C.-V. Mihali, C. Oprean, V. Serafim, R.A. Popovici, C.A. Dehelean, The cytotoxic effects of betulin-conjugated gold nanoparticles as stable formulations in normal and melanoma cells, Front. Pharmacol. 9 (2018) 429, https://doi.org/10.3389/fphar.2018.00429.
[30] F. Osaki, T. Kanamori, S. Sando, T. Sera, Y. Aoyama, A quantum dot conjugated sugar ball and its cellular uptake. On the size effects of endocytosis in the subviral region, J. Am. Chem. Soc. 126 (2004) 6520–6521, https://doi.org/10.1021/ja048792a.
[31] R. Bhattacharya, P. Mukherjee, Biological properties of "naked" metal nanoparticles, Adv. Drug Deliv. Rev. 60 (2008) 1289–1306, https://doi.org/10.1016/j.addr.2008.03.013.
[32] W.H. De Jong, W.I. Hagens, P. Krystek, M.C. Burger, A.J. Sips, R.E. Geertsma, Particle size-dependent organ distribution of gold nanoparticles after intravenous administration, Biomaterials 29 (2008) 1912–1919, https://doi.org/10.1016/j.biomaterials.2007.12.037.
[33] B. Fadeel, A.E. Garcia-Bennett, Better safe than sorry: understanding the toxicological properties of inorganic nanoparticles manufactured for biomedical applications, Adv. Drug Deliv. Rev. 62 (2010) 362–374, https://doi.org/10.1016/j.addr.2009.11.008.
[34] P. Brouillard, M. Vikkula, Vascular malformations: localized defects in vascular morphogenesis, Clin. Genet. 63 (2003) 340–351, https://doi.org/10.1034/j.1399-0004.2003.00092.x.
[35] P. Brouillard, M. Vikkula, Genetic causes of vascular malformations, Hum. Mol. Genet. 16 (2007) R140–R149, https://doi.org/10.1093/hmg/ddm211.
[36] Y. Wu, M.R. Ali, B. Dong, T. Han, K. Chen, J. Chen, Y. Tang, N. Fang, F. Wang, M.A. El-Sayed, Gold nanorod photothermal therapy alters cell junctions and actin network in inhibiting cancer cell collective migration, ACS Nano 12 (2018) 9279–9290, https://doi.org/10.1021/acsnano.8b04128.
[37] Y. Liu, P. Bhattarai, Z. Dai, X. Chen, Photothermal therapy and photoacoustic imaging via nanotheranostics in fighting cancer, Chem. Soc. Rev. 48 (2019) 2053–2108, https://doi.org/10.1039/C8CS00618K.
[38] J. Song, J.-B. Pan, W. Zhao, H.-Y. Chen, J.-J. Xu, Gold nanorod-assisted near-infrared light-mediated regulation of membrane ion channels activates apoptotic pathways, Chem. Commun. 56 (2020) 6118–6121, https://doi.org/10.1039/D0CC01858A.